Ab initio based examination of the kinetics and thermodynamics of oxygen in Fe-Cr alloys

Adib J. Samin,[1,*] David A. Andersson,[1] Edward F. Holby,[2] and Blas P. Uberuaga[1,†]
[1]*Materials Science and Technology Division, Los Alamos National Laboratory, Los Alamos, New Mexico 87545, USA*
[2]*Sigma Division, Los Alamos National Laboratory, Los Alamos, New Mexico 87545, USA*

(Received 12 February 2019; revised manuscript received 23 April 2019; published 15 May 2019)

The behavior of oxygen in Fe-Cr binary alloys is important to understand for a variety of applications including fuel cell interconnects and nuclear energy systems. In this work, we performed an *ab initio* investigation of the binding of oxygen in the entire compositional range of Fe-Cr at minima and saddles. This database was subsequently used to parametrize concentration-dependent local cluster expansions which were utilized to examine the kinetics of oxygen transport in the alloy and the thermodynamics of the system. The behavior of oxygen in the alloy system was investigated using our cluster expansion model and a convex hull diagram was recorded. The most favorable composition for the incorporation of oxygen was found to occur at 70% Cr. The dependence of the oxygen solution energy on the Cr occupation of the nearest neighbor shells was carefully characterized. It was determined that the third nearest neighbor Cr occupation was unfavorable and that, generally speaking, the first and second nearest neighbor shell Cr occupation was favored with a few exceptions. Kinetic Monte Carlo models at dilute oxygen levels were performed using two models [a kinetically resolved activation (kRA) model and a cluster expansion model for the saddle points]. The models qualitatively agreed with the observed trends in the literature which reported a decrease in diffusivity at dilute Cr levels, but the models predicted different behaviors beyond the dilute Cr limit. Finally, using grand canonical Monte Carlo, we further examined the thermodynamics of oxygen incorporation into the alloy. Together, our results offer new insight into the behavior of oxygen in Fe-Cr alloys that have ramifications on the early stages of the corrosive behavior of the material.

DOI: 10.1103/PhysRevB.99.174202

I. INTRODUCTION

Fe-Cr binary alloys are the base components for many ferritic steels which are commonly used for their low cost, good ductility, corrosion and radiation resistance, and thermal stability. Furthermore, these systems display complex behavior which varies considerably as a function of composition ranging from spin glass to magnetoresistance [1–3]. Due to their favorable characteristics, these materials have become the focal point for many potential technological applications including interconnects for high-efficiency solid oxide fuel cells [4,5] and structural components for future nuclear energy systems such as Generation IV fission reactors and fusion reactors [6–8].

The introduction of foreign atoms such as oxygen or hydrogen into the system may occur during fabrication, or during the functional operation of the material and these atoms may significantly impact the properties of the material and affect its performance. Therefore a number of investigators have recently attempted to study and better characterize the behavior of foreign atoms in such Fe-Cr alloys including studies on the behavior of carbon, hydrogen, boron, helium, and nitrogen [9–13]. Corrosion is one of the major factors which affect the extent of the operational lifetime of Fe-Cr alloys and oxygen diffusion in these materials plays an important role in the early stages of oxide growth [14]. Thus a complete understanding of corrosion requires an examination of oxygen transport in the metal. As a consequence, a number of studies have been performed by investigators over the years to better understand the behavior and kinetics of oxygen in Fe-Cr alloys and metal alloys more generally. Several authors [15–17] who used the oxide as a reference calculated the value of oxygen formation energy (on octahedral interstitial site) to be on the order of 1.3–1.5 eV. The choice of an oxide as reference material is often justified since important experiments such as internal oxidation are performed using an oxide/Fe powder to fix the pressure in an otherwise evacuated chamber.

Wang *et al.* [18] studied the oxidation behavior of 5 wt% Cr (5Cr) ferritic steel in air at high temperatures, demonstrating that the oxidation of these steels is primarily controlled by the inward diffusion of oxygen between 500 °C and 900 °C. Setiawan *et al.* [19] found that the growth of internal oxidation zones in Fe-Cr alloys (up to 5 wt% Cr) obeyed the parabolic rate law, indicating that oxygen permeation was the rate determining step. Furthermore, the authors observed the oxygen permeability to increase linearly with increasing Cr concentration (for the alloys being studied). Takada and Adachi [20] studied oxygen diffusion in bcc Fe by internal oxidation measurements on iron alloys with various contents of silicon in a temperature range from 1073 to 1173 K. The authors concluded that the existence of oxide particles accelerated oxygen diffusion. Idczak [21] used transmission Mössbauer spectroscopy to study internal oxidation kinetics in dilute Fe-Cr alloys. The author reported activation energies of 0.46 and 0.6 eV for the internal oxidation process of

*Current address: Department of Engineering Physics, Air Force Institute of Technology, 2950 Hobson Way, Wright-Patterson Air Force Base, Ohio 45433, USA.
†blas@lanl.gov

$Fe_{0.97}Cr_{0.03}$ and $Fe_{0.94}Cr_{0.06}$, respectively, and that the internal oxidation slowed with increasing Cr content. The author also reported that the parabolic oxide growth law was not valid in this regime, i.e., that diffusion was not the rate limiting step for oxide growth. Zeng *et al.* [22] utilized machine learning to study interstitial oxygen diffusion in different metals. The authors reported activation energies of 0.94 eV and 1.44 eV for oxygen diffusion in bcc Fe and bcc Cr, respectively. They attributed these high values to the binding of oxygen to metal vacancies. Wang *et al.* [23] performed DFT and atomistic kinetic Monte Carlo simulations to examine the influence of dilute substitutional atoms ($\leqslant$2 at%) on the diffusion of oxygen. The authors observed that oxygen was most energetically favorable at octahedral sites and that tetrahedral sites were the saddle points for migration and reported that the presence of Cr ($\leqslant$2 at%) caused a significant reduction in the mobility of oxygen. The authors further concluded that the inclusion of foreign substitutional atoms (such as Cr) led the oxygen diffusion coefficient to show deviations from the Arrhenius law.

A number of studies on oxygen behavior have also been conducted on other metals and alloys. Velho and Bartlett [24] examined the diffusivity of oxygen in platinum and platinum-nickel alloys at high temperatures (1400 °C–1500 °C). In their study, the authors used smaller amounts of nickel than required for internal oxidation and concluded that the nickel solute had negligible effects on oxygen diffusion. Perkins and Padgett [25] investigated oxygen diffusion in Zr-Nb alloys ($\leqslant$1 wt% Zr). The authors observed the diffusivity to decrease with increasing Zr concentration and argued that the Zr atoms formed trapping sites at which O-Zr clusters may be formed. Ross *et al.* [26] performed a first-principles study on oxygen diffusion in Al. The authors found that vacancies played a negligible role in migration and reported a curved minimum energy pathway with an energy barrier of 0.95 eV. Kim *et al.* [27] utilized first-principles calculations to study interstitial oxygen diffusion in nickel and nickel chromium binary alloys (12.5 at% Cr). The authors found that oxygen favored octahedral sites and their calculated activation energies for the diffusion of oxygen in Ni-Cr binary alloy showed lower values than in nickel. They reported oxygen diffusion coefficients of 2.4×10^{-13} m^2/s at 1000 °C and 1.74×10^{-15} m^2/s at 1000 °C in nickel and the Ni-Cr (12.5 at.%) binary alloy, respectively. The authors realized that this result was in contradiction with the available experimental observations in the literature, which reported a decrease in oxygen diffusion with increasing Cr content and explained this apparent contradiction by the fact that their model did not account for oxide formation.

From these studies, it emerges that oxygen favors binding at octahedral sites of bcc iron with tetrahedral sites acting as saddle points for diffusion. Furthermore, it appears that, in most cases reported, oxide growth is diffusion-controlled and limited by inward diffusion of oxygen and that the mobility of oxygen in iron was reduced when small amounts of Cr were incorporated into the metal structure. Despite all these studies, several questions remain unanswered. Most of the previous studies were limited to oxygen behavior in pure metals and only a few studies examined oxygen behavior in alloys. Moreover, most of the studies that examined alloys were limited to relatively small concentrations of the alloying element in the metal. Thus it is important to develop a comprehensive understanding of the kinetics and thermodynamics of oxygen in the alloys as a function of the alloy composition due to the role these processes may play in the early stages of oxide growth. Establishing an understanding of the mechanisms underpinning oxygen behavior in metallic alloys is also crucial for achieving an optimal design of corrosion-resistant materials and efficient fuel cells. This knowledge is particularly relevant for heterogeneous structures arising from chromium-rich and chromium-depleted regions that may arise due to radiation-induced segregation or the formation of chromia scales at the exposed metal surface [28–30].

In this work, we utilized a series of density functional theory (DFT) calculations to calculate the oxygen solution energy for minima and saddles in different Fe-Cr environments. These results were subsequently used to train concentration-dependent local cluster expansion (CDLCE) models which were finally used to study the kinetics and thermodynamics of the system. We find that the behavior of oxygen in these alloys is very complex, deviating significantly from simple "ideal solution" (or linear) interpolation between Fe and Cr limits. Our results provide new insight into the behavior of oxygen in Fe-Cr alloy specifically and metallic alloys more generally.

II. COMPUTATIONAL METHODS

A. DFT calculations

Spin polarized density functional theory calculations were carried out using the Vienna *ab initio* simulation package (VASP) [31] with the implementation of the projector-augmented-wave (PAW) pseudopotentials [32,33]. The generalized gradient approximation (GGA) exchange correlation functional was used as parameterized by Perdew, Burke, and Ernzerhof [34]. The valence electron eigenfunctions were expanded in a plane-wave basis set with an energy cutoff of 500 eV. The Fermi level was smeared using a Methfessel-Paxton smearing of the first order of width 0.05 eV in all calculations [35]. The convergence criterion for the electronic self-consistent calculation was set to 10^{-6} eV. Furthermore, the structure was allowed to relax until the total calculated energy difference between successive calculations was less than 10^{-4} eV.

First, DFT calculations were performed on the unit cells of bcc Fe and bcc Cr in order to determine the optimal lattice constant for the pseudopotentials used. Reciprocal length integrations were performed using a ($18 \times 18 \times 18$) Monkhorst-Pack [36] Γ-centered k-point grid. Next, $3 \times 3 \times 3$ supercells of pure iron, pure chromium and Fe-Cr binary alloys (a total of 54 atoms) were prepared by randomly placing the atoms at the bcc lattice positions. In reality, at larger Cr concentrations, the two metals are immiscible and would phase separate. However, we are interested in the behavior of the solid solution and assume such a state for the entire compositional range, to give insights into the behavior of oxygen in the alloy in the limit of no O-O interactions. Different representations of the alloy were produced by random assignment to allow for chemical variation and improved statistics. Moreover, the atoms were relaxed in the DFT calculation using a $5 \times 5 \times 5$ Monkhorst-Pack Γ-centered k-point mesh while the volume

was kept fixed. The lattice constant used for each calculation was linearly interpolated between the lattice constants of bcc iron and bcc chromium depending on the total composition. The solution energy was computed by using the relaxed DFT calculation for that specific alloy (of composition $Fe_{1-x}Cr_x$ with $0 \leqslant x \leqslant 1$) and half the energy of the oxygen molecule as reference according to the equation:

$$E_{\text{sol}} = E(\text{Fe}_{1-x}\text{Cr}_x\text{O}) - E(\text{Fe}_{1-x}\text{Cr}_x) - \tfrac{1}{2}E_{\text{O}_2}. \quad (1)$$

This is the same reference used by Claisse *et al.* [37], a reference of oxygen in its native state. The choice of the reference is arbitrary and does not impact the findings in this paper. For each alloy, two different calculations were performed, one with an initial ferromagnetic structure and another with an antiferromagnetic structure owing to the different magnetic orientations of the parent Fe and Cr structures, respectively. The structure with the lower energy was used as the reference state for O solution. Octahedral sites (O sites) were randomly selected and an oxygen solution energy calculation at each selected O site was performed with the same parameters as the reference (fixed interpolated volume) with the final magnetic moments of the relaxed lattice used as an initial guess for the DFT calculations with oxygen.

Finally, climbing image nudged elastic band (CI-NEB) calculations [38] were used in order to identify the transition state for O migration between sites. A $4 \times 4 \times 4$ k-point mesh was utilized here to reduce the computational cost. One image between the two O-site end states was utilized and the calculations were terminated when the total force on each atom dropped below 0.01 eV/Å.

B. Localized cluster expansion and kinetic Monte Carlo

Following the procedure outlined by Qin and Jiang [39], a concentration-dependent local cluster expansion (CDLCE) about the octahedral site was performed in order to study the behavior of oxygen in the entire compositional range of Fe-Cr alloys. In this method, the local environment was characterized by a local cluster expansion of the form:

$$E_{\text{sol},i} \equiv E_{\text{sol}}{}^{\text{CE}}(\boldsymbol{\sigma}, x) = J_o(x) + \sum_{\alpha} m_\alpha J_\alpha(x) \left\langle \prod_{i \epsilon \alpha} \sigma_i \right\rangle, \quad (2)$$

where the sum in Eq. (2) runs over all symmetrically inequivalent clusters. In the local cluster expansion, equivalent clusters are derived by applying point symmetry operations about the octahedral site. $E_{\text{sol},i}$ represents the solution energy of the ith O site and is short-hand notation for the more general dependence on $\boldsymbol{\sigma}$ and x. Each lattice site (i) is assigned an occupation variable $\sigma_i = +1$ or -1 depending on whether it is occupied by an Fe (-1) or a Cr ($+1$) atom. The angular brackets indicate an average being taken for all clusters symmetrically equivalent to cluster α to yield correlation functions. These correlations are normalized (through averaging over equivalent clusters) and their values are restricted between (-1) and ($+1$). In the equation, m_α accounts for the multiplicity of the cluster α. In Eq. (2), x represents the overall fraction of Cr in the alloy and the J values represent the effective cluster interactions (ECIs) for the interaction of an oxygen at the octahedral site with a cluster of neighboring metal atoms. J_0 represents the zero-metal neighbor (one-body) cluster that physically corresponds to the oxygen occupying an O site without interactions with any surrounding metal atoms (Fe or Cr), J_1 represents a one-metal neighbor (two body) cluster [physically corresponding to one metal atom lattice site in the figure which could be occupied by a Cr atom ($+1$) or an Fe atom (-1)] and so on. In our case, a figure consists of an octahedral site occupied by an oxygen atom and a cluster of neighboring metal atoms. What is different in the concentration dependent methodology is that the effective cluster interaction energy parameters are assumed to be linear functions of the overall composition. This local cluster expansion was then fit to the oxygen solution energy from the DFT database including 103 relaxed structures encompassing many different alloy compositions (with randomized structures). The cluster expansion model was first parametrized using 65 different solution energies and a Monte Carlo simulation was performed to search for the lowest solution energy configurations. The output of our Monte Carlo simulation was subsequently used as input for a new DFT calculation and added to the database. This process was repeated a number of times resulting in a DFT database containing a total of 103 O solution energies for varied binary alloy structures. In this work, the cluster expansion consisted of one one-body term, five two-body terms (up to the fifth nearest neighbor), five three-body terms (encompassing first and third nearest neighbors), four four-body terms, three five-body terms, two six-body terms, and one seven-body term (including the two first nearest neighbors and the four second nearest neighbors). The "neighbor" in our formulation refers to the metal atom bcc site neighboring the octahedral site. The clusters were chosen to be localized about the oxygen atom site and a cluster was not included in the basis set unless all its underlying subsets of clusters were already used in the expansion. Furthermore, it is important to note that the cluster expansion prediction of the oxygen solution energy does not yield any information about the stability of the alloy.

C. Kinetics

kMC simulations were performed to determine oxygen transport properties for different alloys. Two different models were used in constructing the saddle-point energy landscape. In the first, we utilized a kinetically resolved activation barrier model [40–42] to determine the barrier height. Our implementation of the model is described elsewhere [13]. However, the description of this equation is shown again here as there was an error in the equation (not the implementation) reported in our previous work:

$$E_{\text{barrier}}(i \to j) = \begin{cases} \frac{E_{\text{sol},j} - E_{\text{sol},i}}{2} + E_o, & |E_{\text{sol},j} - E_{\text{sol},i}| \leqslant \frac{|E_{\text{sol},j} - E_{\text{sol},i}|}{2} + E_o \\ E_{\text{sol},j} - E_{\text{sol},i} + 0.01\ \text{eV}, & E_{\text{sol},j} \geqslant E_{\text{sol},i} \text{ and } |E_{\text{sol},j} - E_{\text{sol},i}| \leqslant \frac{|E_{\text{sol},j} - E_{\text{sol},i}|}{2} + E_o \\ 0.01\ \text{eV}, & E_{\text{sol},i} \geqslant E_{\text{sol},j} \text{ and } |E_{\text{sol},j} - E_{\text{sol},i}| \leqslant \frac{|E_{\text{sol},j} - E_{\text{sol},i}|}{2} + E_o \end{cases}. \quad (3)$$

The second kMC model was implemented by producing another composition-dependent local cluster expansion to capture the behavior of the solution energy of the saddle points (SPs). This cluster expansion was fitted to a relatively small database consisting of 16 saddle-point energies identified via climbing-image NEB DFT calculations. The first ten saddle points were randomly chosen as follows. The first two calculations were performed on bcc Fe and bcc Cr. After that, two calculations were performed in each of the following compositional structures 10%, 20%, 50%, and 90% Cr. We then used the saddle point data to parametrize our model and used our model to search for the lowest energy saddle points in the following structures: 60%,70%, 20%, 2%, 17%, and 93% Cr. Each was subsequently added to the database and the parameters were recalculated. These structures were already used in our DFT calculations to calculate several octahedral site solution energies. We used the parametrized saddle point model to search all the saddle points of these supercells and added the lowest energy ones to the database. Subsequently, with available cluster expansions to describe both the oxygen solution energy at the minima and the saddle points (SPs), the barriers for hopping were calculated *a priori* as follows:

$$E_{\text{barrier}}(i \to j) = \begin{cases} E_{\text{sol}}(\text{SP}) - E_{\text{sol},i}, \; E_{\text{sol}}(\text{SP}) \geqslant E_{\text{sol},k} \text{ for any k} \in \text{first nn of SP} \\ E_{\text{sol}}(\text{SP}) = \max(E_{\text{sol},k}) + 0.01 \text{ eV}, \; E_{\text{sol}}(\text{SP}) \leqslant E_{\text{sol},k} \text{ for any k} \in \text{first nn of SP} \end{cases}. \tag{4}$$

In Eq. (4), $E_{\text{sol}}(\text{SP})$ represents, per Eq. (2), the solution energy of oxygen at the saddle point (SP) (which in our case is the tetrahedral site in agreement with previous works referenced above). The first nearest neighbors of the SP in our case are O sites [10].

In our model, the octahedral sites were determined to be energy minima, and the tetrahedral interstitial sites the saddle points, consistent with previous work [22]. Only hops between first nearest neighbor octahedral sites (distance $a/2$ apart) were considered in the model since it was observed by Wang *et al.* [23] that oxygen hops between second nearest neighbor octahedral sites (distance $a/\sqrt{2}$ apart) were found to consist of two first nearest neighbor O site hops and the barrier for an O hop between third nearest neighbor O sites was shown to have a relatively large barrier (almost 3 times as high as the first nn O site hops) [22]. The attempt frequency was linearly interpolated between the pure iron and pure chromium hop frequencies depending on the total composition. These attempt frequencies for each element were calculated in the same $3 \times 3 \times 3$ bcc supercells by locating the two first nearest neighbor metal atoms to the O site and the four first nearest neighbor metal atoms about the T site, displacing the same atoms in both calculations by 0.1 Å and utilizing a $4 \times 4 \times 4$ k-point mesh to reduce the computational cost. In these calculations, the criteria for terminating the electronic self-consistent loop was that the energy difference fall below 10^{-7} eV.

D. Thermodynamics

Monte Carlo simulations were employed utilizing the DFT-based cluster expansion model for representing the oxygen solution in Fe-Cr alloys. Two types of equilibrium Monte Carlo simulations were performed. The first was a Monte Carlo simulation in the grand canonical ensemble (GCMC), where the chemical potential was fixed and the number of oxygen atoms in the system was allowed to fluctuate. This type of ensemble allowed us to record the oxygen solution isotherms and to track the evolution of the bound oxygen profiles. The second was a fixed occupation Monte Carlo simulation containing only one oxygen atom and a fixed alloy composition. In this type of simulation, the configuration of the metal atoms around the oxygen was allowed to vary between Fe and Cr with the constraint that the total number of Cr atoms in the system was fixed. The classic Metropolis algorithm was utilized for both, but the insertion and deletion probabilities for GCMC simulation had different prefactors associated with them as described by Tuckerman [43]. In the first simulation, an octahedral site is randomly chosen. If the site is already occupied by an oxygen atom, then particle deletion occurs at a probability of

$$P_{\text{del}} = \min\left\{1, \frac{\lambda^3 N}{V} e^{-\beta\mu} e^{-\beta(E'-E)}\right\}. \tag{5}$$

If the O site was empty, then the insertion probability was calculated as follows:

$$P_{\text{ins}} = \min\left\{1, \frac{V}{\lambda^3 (N+1)} e^{\beta\mu} e^{-\beta(E'-E)}\right\}, \tag{6}$$

where V is the volume of the simulation box and N is the total number of particles prior to attempting a move, E' is the energy of the system following an insertion or deletion, and E the energy of the system prior to attempting an insertion or deletion. Here λ is the de Broglie thermal wavelength of the oxygen calculated from

$$\lambda = \sqrt{\frac{2\pi\hbar^2}{m k_B T}}, \tag{7}$$

where m is the mass of an oxygen atom.

In our implementation of the model the energy differences were calculated as follows:

$$E' - E = \Delta N\left(E_{\text{sol},j} + \tfrac{1}{2}E_{\text{O}_2}\right), \tag{8}$$

where $\Delta N = +1$ in the case of insertion and -1 in the case of deletion, and $E_{\text{sol},j}$ is the solution energy of oxygen at site j calculated from the cluster expansion. This difference contains the term $\frac{1}{2}E_{\text{O}_2}$ on the right-hand side. This is a direct consequence of the definition of the solution energy in Eq. (1). A different choice for the reference would have led to a different term here and this term has no relation to the oxygen chemical potential which is an important parameter in our simulations which controls the quantity of oxygen in the alloy.

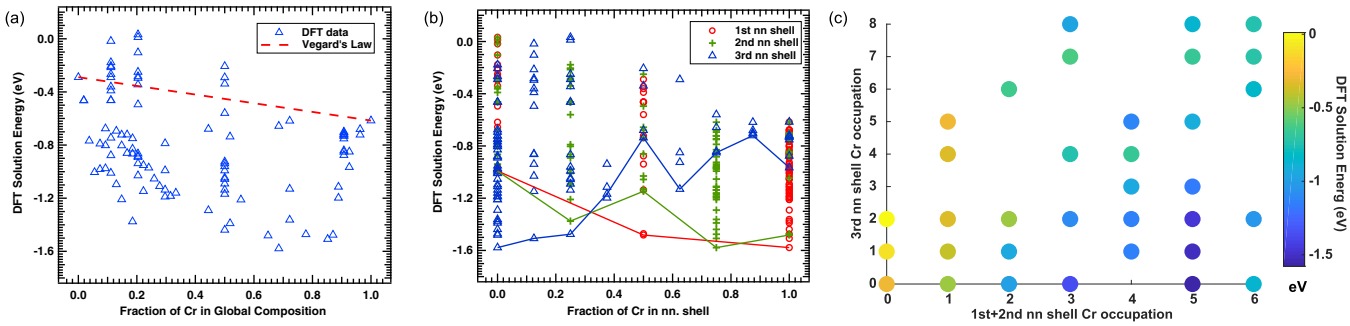

FIG. 1. (a) Variation of the DFT-calculated oxygen solution energy as a function of the global composition of the host alloy. The line represents a linear interpolation between pure Fe and Cr. (b) The DFT-calculated oxygen solution energy as a function of the Cr fractional occupation of the nearest neighboring shells of the occupied O site. A line connects the lowest energy data points for each shell to help guide the eye. (c) The dependence of the lowest DFT-calculated oxygen solution energy configurations in the database on the fractional Cr occupation of the combination of first+second shell and third nearest neighboring shells.

III. RESULTS

A. The DFT database

A systematic investigation of pure bcc iron revealed an optimal lattice constant of 2.83 Å and a ferromagnetic state with a magnetic moment of 2.2 μ_B/atom. A similar investigation of Cr led to an optimal lattice constant of 2.87 Å and a preferred antiferromagnetic arrangement with a magnetic moment of 1.19 μ_B/atom (and a net magnetic moment of zero), consistent with the available literature [44]. When building the DFT database for oxygen binding in the alloy structures, the lattice constant used was linearly interpolated between that of bcc Fe and bcc Cr based on the total composition. As stated, we tried multiple magnetic arrangements and used the lowest energy arrangement to build the DFT database. It was found that starting with a ferromagnetic arrangement always led to more stable structures until we encountered Cr-rich alloys (around 90% Cr) where starting from an antiferromagnetic arrangement led to an energetically more favorable arrangement of the magnetic moments. The results of our systematically assembled DFT database for the oxygen solution energy, as a function of the global Cr composition of the host alloy, are included in Fig. 1. The solution energy for the oxygen at the O site of bcc Fe and Cr was determined to be exothermic in both cases, with values of −0.29 and −0.62 eV, respectively. We note that the zero-point energy correction was estimated to be on the order of 0.03 eV when a calculation was performed by displacing the oxygen atom alone in six directions. As a result, the zero-point energy corrections were assumed not to play a major role in O solution energetics and were not accounted for in this work.

Figure 1(a) shows counter-intuitive behavior and illustrates the breakdown of "ideal solution" behavior (where the solution energy is linearly interpolated between the two endpoints). In particular, our DFT calculations reveal that oxygen strongly prefers mixed Fe-Cr environments to either pure Fe or Cr structures. The most stable environments are those that have a global composition of 70%–80% Cr. Figures 1(b) and 1(c) show the dependence of the oxygen solution energy on the local Cr composition, or Cr occupations of the nearest neighboring shells surrounding the O site where the oxygen is bound. Figure 1(b) reveals that the most stable oxygen solution configurations in our database become more stable with increasing the Cr occupation of the first nearest neighbor (nn) shell and the second nearest neighbor shell but less stable with increasing Cr occupation of the third nn shell. This behavior is rather interesting and unexpected. However, these trends are consistent with the results obtained by Wang *et al.* [23]. In that study, the authors substituted one of the Fe atoms in a supercell with a Cr atom and then calculated the solution energy of oxygen as a function of distance from the Cr atom. They observed that the strongest attraction occurred for the first nearest neighbor, and that the second nearest neighbor was also attractive, but the third nearest neighbor appeared to be repulsive and associated with an endothermic solution energy. However, while these general trends hold here, the behavior appears more nuanced. For example, looking at Fig. 1(c), we find that going from a 7/8 Cr-occupied third nn shell to a fully Cr-occupied third nn shell is associated with a slight energy stabilization whereas going from a 5/6 Cr occupation of the first+second nn shells to fully Cr-occupied first+second nn shells is associated with a slight increase in energy (destabilization). Thus fully Cr-rich structures are not the most energetically favored for O solution.

B. Fitting the local cluster expansion

To understand the ramifications of the physical behavior described above on the thermodynamic and kinetic behavior of oxygen in the alloy, the DFT-generated database was used to parametrize the local cluster expansion. Figure 2(a) shows a good agreement between the concentration-dependent local cluster expansion (CDLCE) and the DFT database along the entire compositional range. Figure 2(b) depicts parity plots for both the CDLCE model (42 parameters) and the concentration-independent LCE model (21 parameters). This plot shows that the scatter about the $y = x$ line is smaller for the CDLCE model and consequently the root mean square error (RMSE) is smaller. The calculated RMSEs for the CDLCE and LCE models are 0.076 and 0.14 eV respectively. The parameters of the fit are included in an Appendix.

Finally, Fig. 2(c) illustrates the predictive power of the two models by showing the spread of errors which results from calculating the leave-one-out cross validation (LOOCV) score. This quantity is calculated by systematically leaving each one of the data points out of the training set, fitting

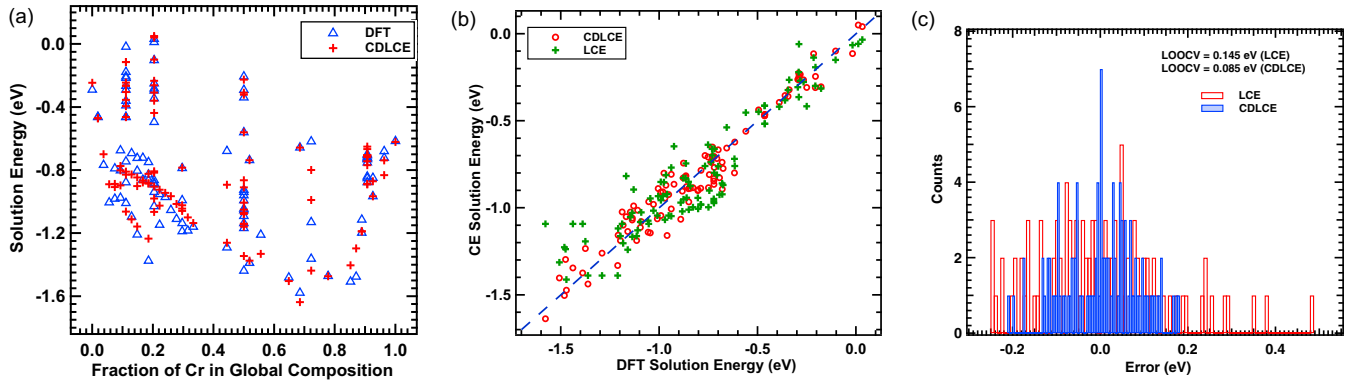

FIG. 2. The fitting of the cluster expansion to the DFT database. (a) The agreement between the concentration-dependent localized cluster expansion (CDLCE) and the DFT database along the entire compositional range. (b) A parity plot comparing the outcome of the CDLCE model with that of the concentration-independent LCE model. (c) The spread of error from calculating the leave-one-out cross validation score (LOOCV) for both the CDLCE and LCE models.

the parameters, then using those parameters to predict the data point that was left out. The LOOCV score recorded for the CDLCE model is almost half that for the LCE model. Therefore, because the number of parameters doubles by introducing a global composition dependence (from 21 parameters to 42 parameters), there appears to be a significant improvement in the performance of the model and this result is consistent with Qin and Jiang's observations [39]. Therefore we will use this model for the remainder of the present work.

C. Kinetics

Each kMC simulation utilized a $20 \times 20 \times 20$ random alloy supercell with periodic boundary conditions. Moreover, interactions between the oxygen atoms were completely ignored in our model. This assumption may be justified in the dilute oxygen limit which is physically most relevant as higher oxygen concentrations have a tendency to form oxides. For each simulation, the trajectory of an oxygen atom was tracked over a minimum of 1×10^7 time steps. This process was repeated 100 times and averaged. This process was further repeated three times for three different representations of the alloy at the same composition to account for random variations in the atomic configuration of the alloy. In these simulations, the attempt frequency for oxygen in each alloy configuration was kept fixed throughout the simulation. This frequency was linearly interpolated between the hop frequencies determined for bcc Fe and bcc Cr, based on the total composition. The hop frequencies in the pure metals were computed via the Vineyard approach [45] by displacing the oxygen atom, the four first nn metal atoms of the O site and the two first nn metal atoms of the T site (the saddle), resulting in hop frequencies of 6.47 and 1.41 THz for oxygen hopping between interstitial O sites in bcc Fe and Cr, respectively. Wang *et al.* [23] reported a vibrational frequency of 15.76 THz in the high-temperature limit. This is likely a consequence of the fact that the authors displaced all atoms in their calculation of the Hessian while we only displaced a subset of atoms. On the other hand, Jiang and Carter [46] calculated a vibrational frequency of approximately 6.5 THz for the hopping of interstitial carbon between octahedral sites. However, we do not expect this issue to impact the results reported in this work. From the CINEB calculations, we obtained an energy barrier of 0.451 eV for oxygen migration in bcc Fe which is consistent with the available literature reporting values between 0.48 and 0.6 eV [15,23,37,47]. The calculated energy barrier for bcc Cr was 0.81 eV and there is no data in the literature, as far as we are aware, to compare this number to.

As mentioned above, two energetic models were used to parameterize the kMC. Figure 3 contains the results for the changes in diffusivity as a function of composition and temperature as predicted from the kinetically resolved activation (kRA) model [as shown in Eq. (3)]. The errors were calculated by propagating the RMSE from the CDLCE.

These results appear to show that even small additions of Cr lead to a significant reduction in the diffusivity up to about 20% Cr. After that the diffusivity remains rather constant until about 90% Cr when there is another significant change in the diffusivity and it increases to its value in bcc Cr. These results are consistent with observations made by Wang *et al.* [23] who conducted a first-principles calculation on a supercell with dilute Cr concentrations, calculated each relevant barrier via DFT, and reported a reduction in oxygen diffusivity with dilute concentrations of Cr (<2 at%). The authors in that work found a drop in the diffusivity by about an order of magnitude from about 10^{-12} m^2/s for pure Fe to about 10^{-13} m^2/s for 1.852% Cr at 500 K. This behavior of the diffusivity of oxygen in Fe-Cr alloys—where it drastically decreases when substituting a few atoms in pure bcc Fe with Cr and significantly changes again near the pure Cr limit—has been observed by other recent studies employing kRA models to analyze diffusion [12,13].

To understand how the diffusivity depends on the treatment of saddle point energies, another set of kMC simulations was performed by first building a cluster expansion representation for the solution energy of the saddle points. Again, we compared a concentration-dependent local cluster expansion with a concentration-independent one. The results can be found in the parity plots in Fig. 4(a). It can be clearly seen that the concentration-independent CE leads to significant scatter. It should however be mentioned that we were limited to a rather small database for the saddle points due to the significant

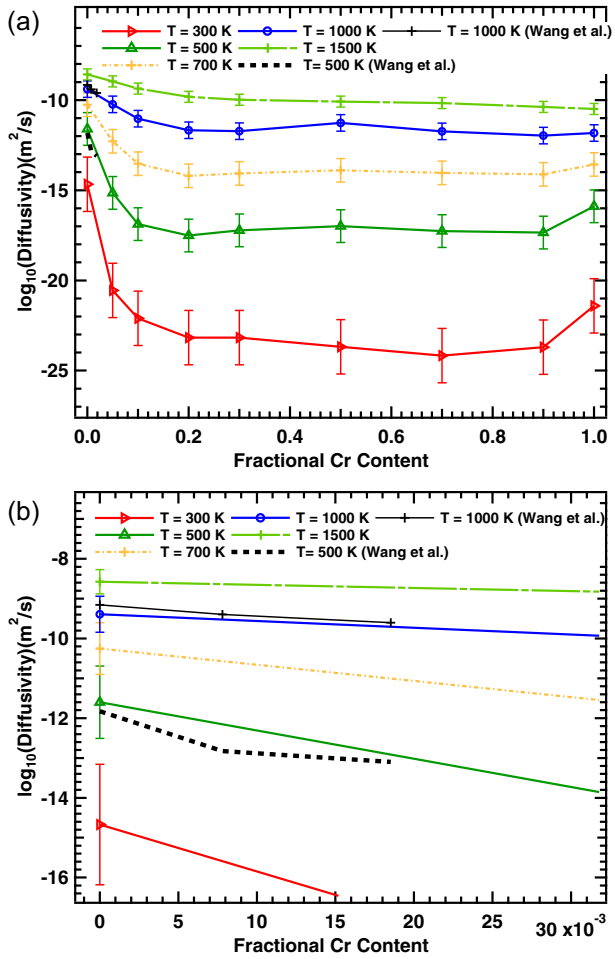

FIG. 3. The kRA model-derived diffusivities [based on Eq. (3)] for multiple temperatures shown across the entire compositional range along with error bars. (a) shows the results for the entire compositional range while (b) highlights a compositional range from 0 to 3% Cr, to emphasize the comparison with the results of Ref. [23].

computational costs associated with NEB calculations. Fitting another CDLCE model to the saddle point solution energies, to the 16 DFT-calculated saddle point solution energy data points, yielded an RMSE of 0.016 eV and a LOOCV score of 0.014 eV. This fit is illustrated in Fig. 4(a). The parameters are included in Appendix. This model was then utilized in a second series of kMC simulations following the procedure outlined in the computational methods. The results of the model based on Eq. (4) are included in Fig. 4(b) and they are drastically different from the predictions of the kRA model by several orders of magnitude.

Again, we see an initial drop in the diffusivity for Cr concentrations up to 20% Cr but the diffusivity begins to increase after that. In fact, the peak in diffusivity is for intermediate compositions at about 60% Cr. Furthermore, the initial drop in the diffusivity is not nearly as significant as the drop observed in the kRA model. The results in Fig. 4(b) are not nearly as sensitive to temperature as those in Fig. 3. Figure 4(b) also indicates a decrease in the diffusivity after about 90% Cr and thus the behavior near bcc Cr is the opposite of that observed in the kRA model, where a significant increase in diffusivity was found. Interestingly, Herschberg's work [12], which examined carbon diffusion in Fe-Cr alloys, included parity plots for the kinetically resolved model barrier predictions compared with the DFT database. The authors' results indicate fair agreement for the Fe-rich side but significant errors on the Cr-rich side. Therefore, it is possible that the kRA model completely breaks down on the Cr-rich side and that it is important to build a model to accurately capture the behavior of the saddle points in this limit to account for the diffusivity in the entire compositional range in a precise manner. Such a finding is likely applicable to a wide-range of alloys, defects, and their migration barriers.

In our previous work, on hydrogen diffusion in Fe-Cr alloys, the saddle point solution energies were rather small and the diffusivity was, to first order, governed by the solution energies of the hydrogen in different environments. In the case of interstitial oxygen, however, we observe in Fig. 4(a) a wide range in the saddle point solution energies (a range of about 1.2 eV). This variation cannot be ignored and plays a significant role in governing the diffusion of oxygen in these alloys. Thus the addition of a CE for the saddle point and the associated addition of computational cost and complexity is required.

The diffusivities in Figs. 3 and 4(b) were fit to an Arrhenius relationship as shown in Fig. 5 and the fitting parameters are included in Table I. The table shows the activation energies for

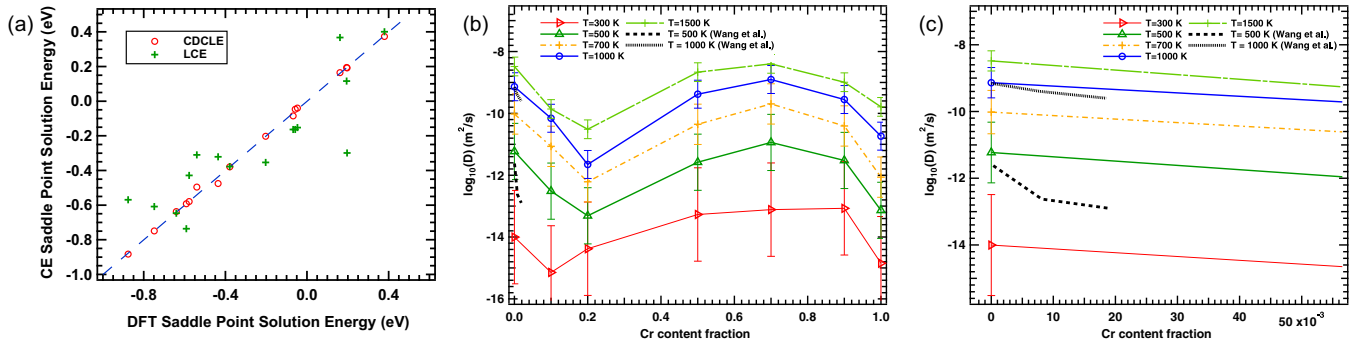

FIG. 4. (a) Parity plot for the cluster expansion fit for the saddle point solution energy database [as determined by Eq. (4)]. Again the results of the CDLCE and the concentration-independent LCE models are included. (b) shows the diffusivities derived from utilizing the parameterized CDLCE model [Eq. (5)] for describing the saddle point solution energies in the kMC simulations while (c) highlights a compositional range from 0 to 5% Cr, to emphasize the comparison with the results of Ref. [23].

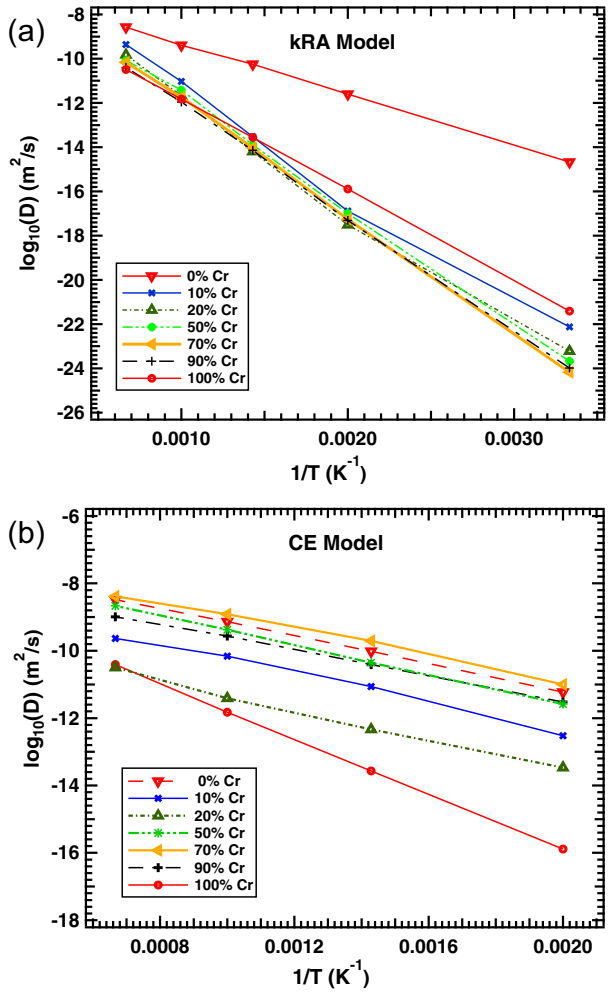

FIG. 5. Arrhenius plots for diffusivity derived from (a) the kRA model and (b) the CE model (where the solution energy of the saddle points was captured through a cluster expansion).

the kRA model monotonically increasing from 0%Cr to about 70% Cr and then decreasing to the activation energy value in pure Cr.

In contrast, the values for the CE model show the activation energy values only slightly increasing over the limited compositional range between 0% Cr to 20% Cr and then monotonically decreasing below its value for bcc Fe up to the point of 90% Cr content, at which point the activation energy increases to its value in 100% Cr. The activation energy values for the CE model of pure bcc Fe and Cr are slightly different from those for the kRA model. This may be due to the either statistical noise in the kMC simulations or errors in the fitting of the CE model for the saddle points. The error bars in the activation energies do not take into account the error in determining the diffusivity (the error bars in Figs. 3 and 4), but rather they are a measure of the variation with respect to the randomness of the alloy configuration. From Fig. 5(b), there appears to be some slight departure from Arrhenius behavior for compositions of 10% and 20% Cr with the CE model. This type of behavior is also consistent with previous observations [22] where the authors attributed that observation to "the inhomogeneous distribution of the barrier heights." Finally, the activation energy for oxygen migration in pure Fe is in excellent agreement with the experiments by Idczak [21], though the energy for pure Cr is somewhat higher than the experimental value.

D. Thermodynamics

Finally, we used the cluster expansion combined with GCMC to examine the thermodynamics of oxygen incorporation into the alloy. Several supercells were built consisting of $10 \times 10 \times 102$ unit cells. The concentration was gradually varied from pure Fe to pure Cr and back to pure Fe along the z direction in order to apply periodic boundary conditions (PBC) in all directions. At each z level of the unit cell, the Cr concentration was specified and a number of atoms corresponding to that concentration was randomly chosen and assigned as Cr. This type of geometry was chosen to understand how variations in composition, such as those that might be present near corrosion fronts or due to radiation-induced segregation, impact the distribution of oxygen in the alloy. We note that Fe-Cr solid solutions are not stable through all of this composition range, but we examine them here as a limit on the behavior predicted by the model. A unique cell was created in this way for each value of the chemical potential that was simulated. A grand canonical Monte Carlo (GCMC) simulation was performed on these supercells at two different temperatures, 300 and 1000 K. The results are included in Fig. 6.

In the GCMC simulation, the total occupation was defined as the number of oxygen atoms in the system divided by the total number of available octahedral sites in the entire supercell (61 200 sites). Each simulation was run for 30 000 Monte Carlo sweeps of the octahedral site lattice. A sweep is defined as a number of MC attempts equal to the number of octahedral sites in the system (61 200 attempts). The chemical potential was explored within a window over which oxygen solution occurs for the temperatures of interest. At lower chemical potentials, the occupation is exactly zero for the temperatures being investigated, and at higher chemical potentials, the occupation variable is 1. The results from the first 1000 sweeps

TABLE I. The activation energy and prefactor derived for the kRA model and the model for which a cluster expansion described the solution energy of saddle points (CE). Model 2 displayed significant departure from Arrhenius behavior.

%Cr	0	10	20	50	70	90	100
kRA : E_a(eV)	0.45	0.96 ± .02	0.995 ± .02	1.03 ± .013	1.06 ± .01	1.01 ± .023	0.81
kRA : $D_o \times 10^7$(m^2/s)	0.88	3.6	1.7	3.5	2.8	1.1	0.49
CE : E_a(eV)	0.404	0.42 ± .01	0.44 ± .01	0.42 ± .02	0.39 ± 0.02	0.38 ± 0.01	0.814
CE : $D_o \times 10^7$(m^2/s)	0.79	0.06	0.006	0.06	1.02	0.2	0.2

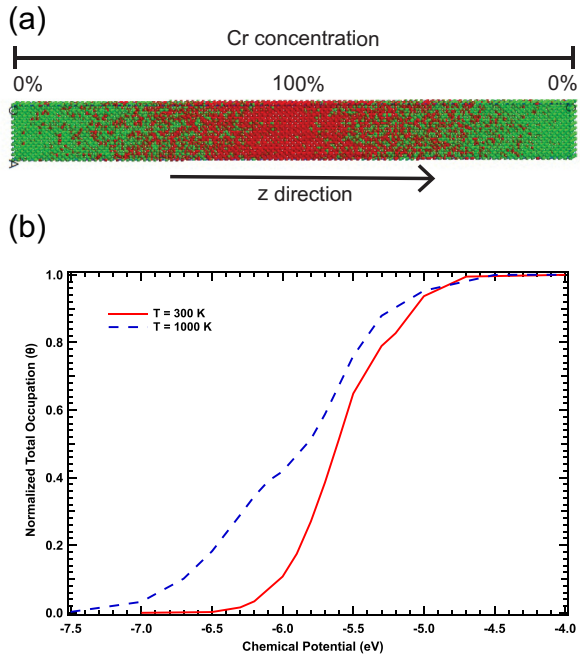

FIG. 6. (a) A representative supercell upon which the grand canonical Monte Carlo simulations of oxygen incorporation were performed. The concentration was gradually varied from pure Fe (green) to pure Cr (red) in the middle and back to pure Fe at the other end in order to preserve PBC. (b) Two isotherms recorded at 300 and 1000 K for the total occupation of oxygen in the entire slab. The total occupation was defined as the number of oxygen atoms normalized by the number of sites in the system.

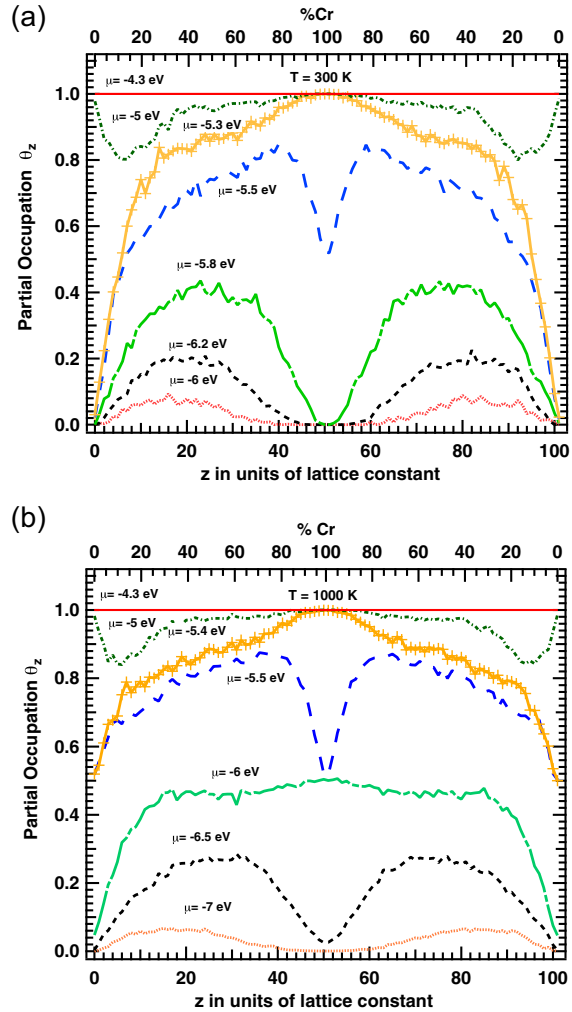

FIG. 7. Profiles of oxygen occupation as a function of z (displayed in units of lattice constants) or, equivalently, Cr composition in the alloy. The partial occupation at each z position was defined as the number of oxygen atoms in the unit cell with the corresponding z position divided by the total number of occupation sites available at each z position (600 sites). (a) shows profiles for $T = 300$ K and (b) shows profiles for $T = 1000$ K. These profiles were averaged over 29 000 Monte Carlo sweeps. The %Cr composition corresponding to the z position is shown on the top x axis for both (a) and (b).

were discarded to allow for equilibration and reported results were obtained by averaging the remaining 29 000 MC sweeps for total O occupation and oxygen concentration profiles. From Fig. 6, we observe that oxygen uptake occurs at a lower chemical potential, corresponding to a lower pO_2, for 1000 K compared with the simulation at 300 K. This behavior is expected as the additional thermal energy at 1000 K allows the system to sample more states for oxygen uptake to occur. While these isotherms may be useful to better inform us about the early stages of oxide growth and incorporation of oxygen, it is important to keep in mind that our model does not take into account the oxygen-oxygen interactions or the phenomenon of oxide formation which occurs at relatively small oxygen concentrations. Therefore the model is valid in dilute oxygen concentrations but is expected to depart from true behavior at higher chemical potentials and oxygen concentrations. In addition, the variable "x" chosen for these calculations was chosen to be 0.5 since the global fraction of Cr in the supercell is 0.5.

Next, the compositional dependence of the oxygen concentration profile was computed as a planar average across a unit cell z level for both T = 300 and 1000 K simulations. These profiles were also averaged over 29 000 steps and the results are shown in Fig. 7.

From examining Fig. 7, it is interesting to notice that the profiles in both simulations change in a similar manner until all the sites are occupied. The oxygen occupation profile shape changes significantly with chemical potential and temperature, with the location of the peak of the profile shifting as a function of the chemical potential.

In an effort to better understand these unexpected changes in the profile shape and the profile peak position as a function of chemical potential, we examined the oxygen solution energy landscape for one of the constructed supercells. This representative landscape of one of the many randomly constructed supercells is illustrated in Fig. 8.

An examination of the landscape in Fig. 8 helps explain the changing shape of the oxygen profiles with increasing chemical potential. The areas consisting of about 50% Cr composition on both sides of the pure Cr region have the lowest energy states and these sites strongly attract the oxygen when it is first introduced into the system. This explains the initial double-hump shape of the oxygen concentration profile

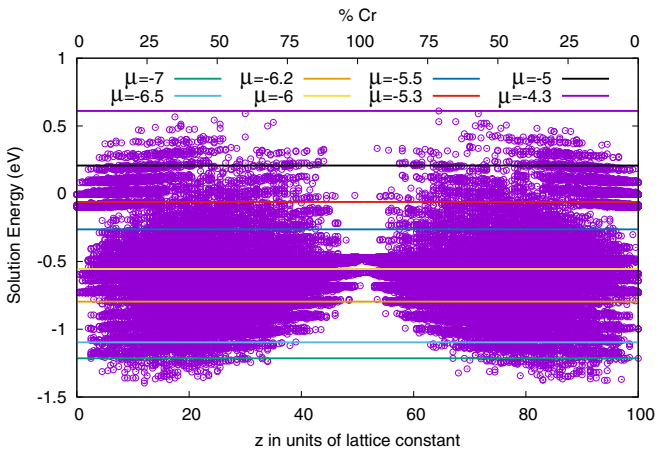

FIG. 8. A representative landscape for the oxygen solution energy in the octahedral sites contained in the supercells being simulated. The Cr composition corresponding to each z level is shown in the top x axis. The lines correspond to the highest occupied energy level at 1000 K corresponding to the indicated chemical potential. The values for the chemical potential are shifted from those of the solution energy by the reference O_2 energy, which is not included in this figure. Figure 8 is to help interpret the behavior in Fig. 7, not to make a concrete connection between the chemical potential and the energy landscape. We would expect similar behavior for $T = 300$ K.

in Fig. 7. Next, as the chemical potential is increased further, the Cr rich region at the center of the simulation geometry suddenly becomes partially filled, corresponding to the flattening of the profile observed for a chemical potential of -6 eV at $T = 1000$ K. This region remains partially-filled as side states are occupied upon further increase in the chemical potential, shifting the peak back towards the 50% Cr regions. Unlike the intermediate- and high-Fe concentration sites, there is only a relatively small variation in solution energy states for the Cr-rich region at the center of the structure. The other half of the central sites is suddenly filled at a chemical potential of -5.5 to -5.4 eV in the 1000 K simulation and the peak again shifts back towards the center of the cell. The last region to start filling is the Fe-rich region at the two ends of the simulation supercell as those are the next available lowest unoccupied energy sites. This precisely corresponds to our observation of the shift in the shape of the energy profile at -5 eV for the 1000 K simulation. Hence, the regions on either end of the simulation which are about 50% Cr are the first regions to attract oxygen and also the last regions to be filled since that region contains both the lowest energy and the highest energy states in the system.

Finally, to obtain further insight into the thermodynamics driving the interaction between oxygen and Cr, we built a $3 \times 3 \times 3$ supercell system of 54 metal atoms, filled one O site with oxygen and performed a canonical Monte Carlo (CMC) simulation at $T = 0$ K for multiple global Cr compositions using our parametrized CDLCE. The goal was to identify the metal atom configuration for a fixed composition which yields the lowest oxygen solution energy. In the process, by tracking the most stable solution energy at each composition, we recorded the hull diagram presented in Fig. 9.

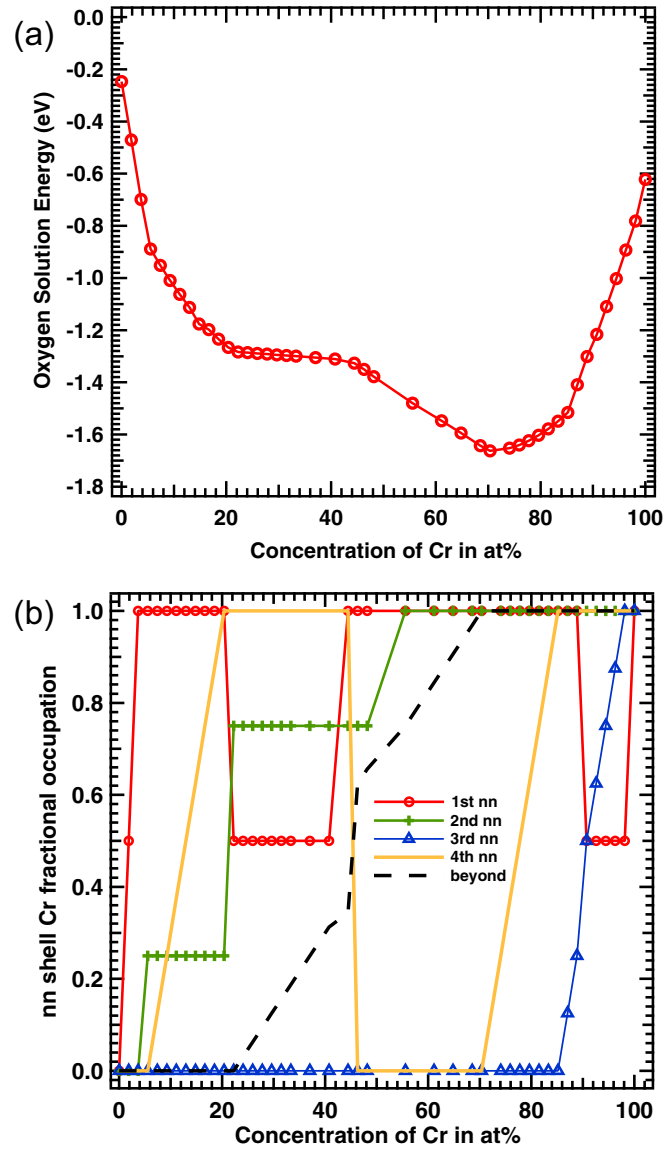

FIG. 9. The results of a canonical Monte Carlo simulation on $3 \times 3 \times 3$ supercells (a total of 54 metal atoms) using the concentration-dependent local cluster expansion (CDLCE). (a) The hull diagram for this supercell at 0 K. The points with the lowest energy configurations at each Cr concentration are shown. (b) The change of the nearest neighbor shell Cr fractional composition as a function of the global Cr composition. The first nn shell contains two metal atoms, the second nn shell contains four metal atoms, the third and fourth nn shells each contain eight metal atoms. The remaining shells contain 32 atoms and, in our notation, are labeled "beyond."

Figure 9(a) illustrates the convex hull diagram obtained by systematically increasing the number of Cr atoms available in the system and searching for the configuration yielding the lowest oxygen solution energy for the composition being examined. The recorded hull flattens at about 10/54 Cr, remaining rather flat until a composition of 20/54 Cr where the oxygen solution energy appears to decrease more until the global minimum, or most stable composition, is attained at a composition of 38/54 Cr. This result indicates that, initially, oxygen in an Fe matrix is stabilized by the addition of Cr but

that this effect saturates somewhat and the oxygen becomes relatively insensitive to further addition of Cr. This happens until sufficient Cr is added, which again further stabilizes the oxygen in the system. Interestingly, as also reflected in Fig. 1, the addition of too much Cr destabilizes oxygen solution.

In Fig. 9(b), the variation of the composition of the nearest neighbor shells as a function of the global composition is recorded. This figure illustrates the complex behavior of the oxygen interaction with the alloy. Some trends however may be extracted. For instance, Fig. 9(b) shows that filling the third nearest neighbor shell with Cr is unfavorable, as was also observed in the DFT calculations described in Fig. 1. This shell is the last shell to start filling. The second nearest neighbor shell appears to be monotonically filling with Cr as we move between a composition of 0 Cr to 54 Cr. Nevertheless, some of the observed behavior is nonmonotonic such as the behavior of Cr occupation of the first and fourth nearest neighbor shells. Near the iron rich limit, the first nn shell appears to favor a totally Cr-filled configuration but it favors a partially filled configuration near the 54 Cr composition. It indeed appears counterintuitive that the configuration which leads to the lowest O-site solution energy in an Fe-Cr_{53} structure is to remove a Cr atom from the first nearest neighbor shell. Similarly, the fourth nearest neighbor shell also displays non-monotonic behavior with respect to its Cr filling.

IV. DISCUSSION AND CONCLUSIONS

It is important to reiterate the limitations of our current study. First of all, even though in some of our simulations we have examined extreme oxygen concentrations, the fidelity of our model is limited to dilute oxygen concentrations without the inclusion of oxygen-oxygen interaction energies or formation of metal oxide structures. This is true for the kinetic simulations where all interactions between oxygen atoms were ignored. This is also particularly true when studying the isotherms recorded from GCMC simulations. Choudhury *et al.* [48] estimated that oxide formation in Fe would begin at a chemical potential of around −6.6 eV for 300 K and −7.1 eV for 1000 K. Therefore it is important to account for oxide formation early in the simulation and this phenomenon would dramatically influence the results of the simulation beyond small oxygen concentrations. Oxide formation is also expected to impact the kinetics of oxygen transport within the alloy. Takada and Adachi [20] reported that oxide particles helped accelerate oxygen diffusion in Fe. However, we include results in the high oxygen limit as it provides further insight into the interaction between oxygen and the metal atoms and serves as a model for other alloy systems where perhaps more oxygen can be incorporated. Furthermore, the role of oxygen-oxygen interactions and the contribution of vacancies in the material to the kinetics and thermodynamics has been completely ignored in the present work. Moreover, it is worth noting that the variable "x" was used as a "global quantity" to parametrize the local cluster expansion referred to the Cr fraction in a 54-atom supercell. However, in the GCMC and kMC calculations, this quantity was defined with respect to a much larger supercell. This may have led to undesired spurious effects such as additional errors in the cluster expansion's prediction power.

In studying the kinetics, the kRA and the CDLCE models led to very different results. Contrary to the predictions of the kRA model, the diffusivity of oxygen initially decreases with Cr concentration but then increases slightly. In an effort to better assess which of the two models is more physical, we compare our results to literature values of other related systems. Whittle and Wood [49] found the oxide growth on Fe-Cr to be diffusion-controlled and reported an increase in the oxidation rate with alloy chromium content. Mandl and Rauschenbach [42] measured the diffusivity of nitrogen in expanded austenite and reported diffusion coefficients on the order of $10^{-14}\,m^2/s$ at 380 °C. Galdikas *et al.* [43] studied nitrogen diffusion through CoCr alloys (20 wt% Cr) through a model based on the linear thermodynamics of irreversible processes, which they compared to experimentally recorded concentration profiles. Fitting their model to the experimental profiles allowed the authors to obtain diffusion coefficients on the order of $10^{-15}\,m^2/s$ at 663 K. Though these systems are not the same as the one studied here, these numbers appear to be closer to the predictions of the CDLCE model, suggesting that this is the more physical model. It should however be emphasized that we were limited to a small database for fitting the solution energy of the saddle points. We used 16 parameters to fit 16 data points and this could have had some ramifications. Finally, Figs. 3 and 4(b) appear to show that the kRA model has better agreement with the results of Wang *et al.* [23], though both models predict the correct overall behavior. However, we speculate that beyond the dilute limit where complex interactions and magnetic effects begin to emerge, the CDCLE model is more physical. The kRA model used here is based solely on solution energies while the model developed by Wang *et al.* is based on the interaction of oxygen with a single solute in the cell. The fact that the CE model deviates from these two suggests that, even in a low-concentration limit of Cr, the saddles are modified by the presence of multiple solutes more than the solution energies. However, further work is needed to fully understand this behavior.

It is useful to examine the ramifications and implications that our results may have on the early stages preceding oxide formation in corrosion processes. From our CMC simulation, we found that local environments of about 20% and 70% Cr are most favorable for the oxygen. These are the sites that atmospheric oxygen may likely bind to at low oxygen pressures. This is likely to be followed by solution to Cr-rich sites and the formation of the Cr_2O_3 scale on the surface of the metal. Similarly, in the case of radiation-induced segregation, oxygen atoms which penetrate the system at low concentrations are likely to be found in mixed Cr-rich environments. That is, oxygen will initially concentrate at intermediate compositions and that is where oxide nucleation may be more likely to initiate. These types of compositions may be most likely those found at microstructural features, such as grain boundaries and dislocations, as the result of radiation-induced segregation. Thus our results suggest that oxygen would first find its way to these regions of the material and initiate oxide nucleation there.

Finally, it is beneficial to emphasize the complex behavior of oxygen interaction with the alloy system as depicted in Figs. 1 and 9. Coming back to Fig. 1, the enhancement in

the oxygen solution energy when increasing the Cr concentration in the alloy is strongly associated with Cr filling of the first nearest-neighbor shell, whereas the enhancement in the oxygen solution energy associated with increasing the Fe concentration in the alloy starting from a pure bcc Cr appears to be initially linked with removing Cr from the first nearest neighbor shell. Thus, the solution energy decreases with increasing first and second shell occupation, but increases with increasing third shell occupation.

More broadly, our results indicate that the interaction of oxygen with metallic alloys is complex. One cannot infer either the kinetic or thermodynamic behavior from knowledge of the behavior in the pure metals. Thus, in developing models of corrosion in these alloys, it is critical to determine the actual compositional dependence of both the thermodynamics and kinetics of oxygen. Our results provide insight into this behavior and lay the foundation for more physical models of how the microstructure of an alloy such as Fe-Cr impacts the corrosive process. Furthermore, our results provide some insight into the early stages of the corrosion process where oxygen transport in the metal is a key parameter in predictions of oxide formation and growth [50]. Our results also provide insight into how oxygen interacts with irradiated alloys in which the composition of the various phases can vary to a much greater extent than indicated by the phase diagram [51].

In summary, a series of DFT calculations were performed on oxygen solution and migration in the Fe-Cr alloy system. The interaction of oxygen with Cr was found to be complex, with oxygen favoring Cr in the first and second nearest neighbor shells but not in the third nearest neighbor shells. Oxygen was further found to hop between first nearest neighbor O sites via T sites, which acted as saddle points. The constructed DFT database at the minima and the saddles was used to parametrize a concentration-dependent local cluster expansion (CDLCE) for oxygen solution energy at both the O sites and T sites. Subsequent kMC simulations using these potential functions revealed that the oxygen diffusivity in the system in the dilute limit first decreased with increasing Cr up to about 20%Cr. This was followed by a slight increase in diffusivity beyond its value in pure bcc Fe in the 20%–90% Cr regime before plummeting again to its value in bcc Cr. These predictions were widely different from simulations based on the kRA model. Moreover, the isotherms for oxygen solution were recorded at 300 and 1000K via a series of GCMC simulations. It was observed that oxygen begins to bind to the alloy system at a much lower chemical potential (lower pO2) when the temperature is elevated and, more interestingly, the peak concentration of oxygen in the system shifted spatially several times as a function of the chemical potential. This observation was explained by examining the energy landscape of the system. Finally, a systematic investigation of oxygen solution in a 54 atom bcc supercell was performed using a fixed occupation MC simulation based on our parametrized cluster expansion for the minima. The recorded hull diagram showed that the most favorable oxygen solution energy occurred at 38/54 Cr composition at a very particular ordering of Fe and Cr. During this investigation, the Cr-occupation of the nearest neighbor shells was tracked and the dependence of the oxygen solution on the Cr-occupation of these shells was further scrutinized in order to understand the relationship of oxygen solution energy and local alloy composition. Our study is mostly relevant for Fe-Cr alloys containing a dilute concentration of oxygen since our model completely ignores oxygen-oxygen interactions and the role of oxide formation, which is known to occur at relatively low oxygen pressure.

ACKNOWLEDGMENTS

This research was primarily supported by the LANL Laboratory Directed Research and Development (LDRD) program (A.J.S., conceptual design of study, development of model and execution of simulations). In addition, E.F.H. and B.P.U. acknowledge support as part of FUTURE (Fundamental Understanding of Transport Under Reactor Extremes), an Energy Frontier Research Center funded by the U.S. Department of Energy (DOE), Office of Science, Basic Energy Sciences (BES) (conceptual design of study, interpretation of

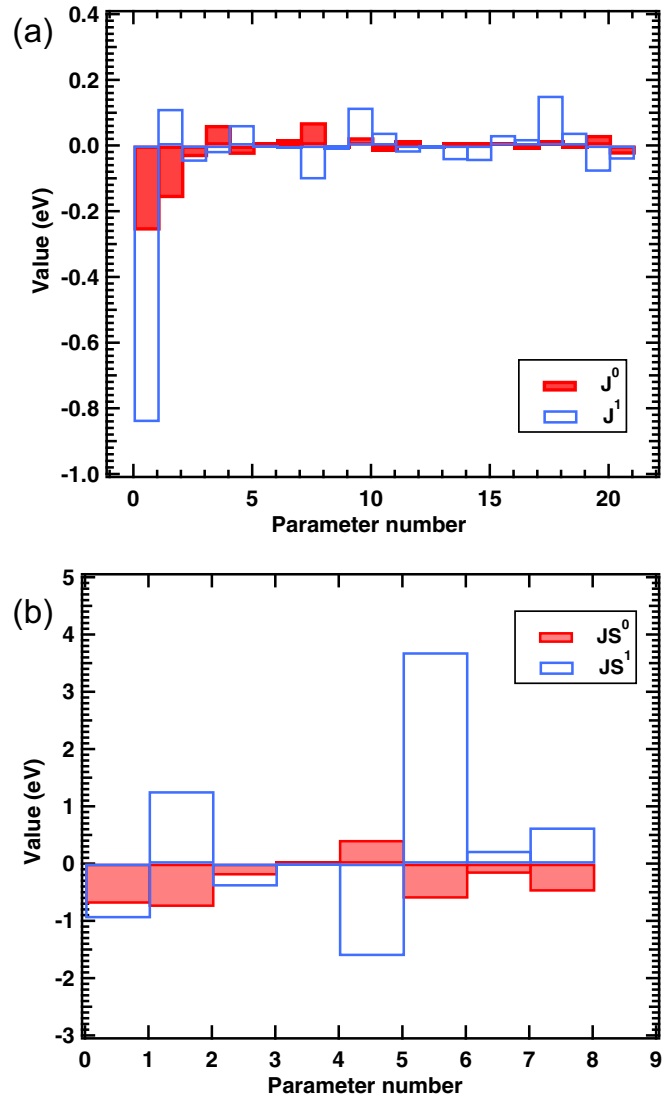

FIG. 10. (a) includes the effective interaction parameters for fitting the oxygen solution energy of the octahedral sites, 42 parameters used to fit 103 data points. (b) includes the effective interaction parameters for fitting the computed saddle points, 16 parameters used to fit 16 data points.

results). AJS primarily wrote the manuscript, but all authors contributed to the writing and editing of the manuscript. Computational support through Los Alamos National Laboratory Institutional Computing is gratefully acknowledged. This work was supported by the US Department of Energy through the Los Alamos National Laboratory. Los Alamos National Laboratory is operated by Triad National Security, LLC, for the National Nuclear Security Administration of U.S. Department of Energy (Contract No. 89233218CNA000001).

APPENDIX

In the CDLCE model, each parameter is a linear function of the fraction of Cr (x) in the global alloy composition. Hence, each parameter may be written as $J_k(x) = J_k{}^0 + J_k{}^1 x$. In this notation, the subscript k indicates the effective interaction of an oxygen atom occupying an octahedral site with a cluster of k metal atoms. The superscripts 0 and 1 represent the constant term and the linear term for each cluster. The values of the parameters for the oxygen solution energies of the octahedral sites are included in Fig. 10(a).

Parameter 0 represents the zero metal neighbor energy parameter, parameters 1 through 5 represent two-body (one metal neighbor) figures up to the fifth nearest neighbor (distances between nn metal atom and O site: first body nn $= 0.5a$, second body $= 0.707a$, third body $= 1.118a$, fourth body $= 1.2247a$, fifth body $= 1.5a$). Here, a represents the bcc lattice constant. It is important to emphasize that the term "neighbor" in our formulation refers to metal lattice sites neighboring the octahedral site in question. Parameters 6 through 10 represent three-body (two-metal atom neighbor clusters) effective interactions. Parameter 6: first+second nn with a maximum distance of $0.866a$. Parameter 7: two first nn (max. dist. $= a$). Parameter 8: two second nn atoms (max. dist. $= a$). Parameter 9: two second nn (max. dist. $= 1.41a$). Parameter 10: first+third nn (max. dist. $= 1.118\,a$). Parameters 11–14 are four-body figures (three neighboring metal atom clusters). Parameter 11: two first nn+ one second nn (max. dist. $= a$). Parameter 12: one first nn+two second nn (max. dist. $= a$). Parameter 13: one first nn+ two second nn (max. dist. $= 1.41a$). Parameter 14: three second nn (max. dist. $= 1.41a$). Parameters 15–17 are five-body figures (four neighboring metal atom clusters). Parameter 15: two first +two second nn.(max. dist. $= a$). Parameter 16: one first+three second nn. Parameter 17: four second nn. Parameters 18 and 19 are six-body figures (five neighboring metal atom clusters). Parameter 18: two first nn+three second nn. Parameter 19: one first nn+ four second nn. Parameter 20 is a seven-body figure (six metal atom neighbor clusters) (two first nn+ four second nn). From examining Fig. 10(a), the value of the parameters tends to get smaller with parameter number. This is an indication that the cluster expansion is converging.

Figure 10(b) shows the parameters derived upon fitting the saddle point oxygen solution energies. Here it is important to distinguish that, contrary to the first cluster expansion which was performed about O sites, this cluster expansion was performed about tetrahedral (T) sites in the lattice. This particular expansion includes, in order, a zero-metal neighbor figure, three two-body figures (one metal atom clusters), and four three-body figures (two metal atom clusters). These figures are the same as described in Table 2 of our previous work [13]. Here we only utilized one-metal neighbor figures up to the third nn and used the first four entries for the two-metal neighbor figures. It is important to emphasize again that, due to the computational costs associated with NEB calculations, our database for fitting the cluster expansion for the saddle point solution energies was rather limited.

[1] A. Kuronen *et al.*, Phys. Rev. B **92**, 214113 (2015).
[2] S. K. Burke, R. Cywinski, J. R. Davis, and B. D. Rainford, J. Phys. F: Metal Phys. **13**, 451 (1983).
[3] P. Grünberg, R. Schreiber, Y. Pang, M. B. Brodsky, and H. Sowers, Phys. Rev. Lett. **57**, 2442 (1986).
[4] R. Sachitanand, M. Sattari, J.-E. Svensson, and J. Froitzheim, Int. J. Hydrogen Energy **38**, 15328 (2013).
[5] J.-J. Choi, J. Ryu, B.-D. Hahn, C.-W. Ahn, J.-W. Kim, W.-H. Yoon, and D.-S. Park, Int. J. Hydrogen Energy **39**, 12878 (2014).
[6] L. Malerba, A. Caro, and J. Wallenius, J. Nucl. Mater. **382**, 112 (2008).
[7] L. K. Mansur, A. F. Rowcliffe, R. K. Nanstad, S. J. Zinkle, W. R. Corwin, and R. E. Stoller, J. Nucl. Mater. **329–333**, 166 (2004).
[8] R. L. Klueh and A. T. Nelson, J. Nucl. Mater. **371**, 37 (2007).
[9] D. J. Hepburn, D. Ferguson, S. Gardner, and G. J. Ackland, Phys. Rev. B **88**, 024115 (2013).
[10] A. Abhishek, M. Warrier, and E. R. Kumar, AIP Conf. Proc. **1512**, 858 (2013).
[11] Y. Zeng, Q. Li, and K. Bai, Comput. Mater. Sci. **144**, 232 (2018).
[12] R. Herschberg, C.-C. Fu, M. Nastar, and F. Soisson, Acta Mater. **165**, 638 (2019).
[13] A. J. Samin, D. A. Andersson, E. F. Holby, and B. P. Uberuaga, Phys. Rev. B **99**, 014110 (2019).
[14] T. Roller and W. Bolse, Phys. Rev. B **75**, 054107 (2007).
[15] C. L. Fu, M. Krčmar, G. S. Painter, and X.-Q. Chen, Phys. Rev. Lett. **99**, 225502 (2007).
[16] Y. Jiang, J. R. Smith, and G. R. Odette, Phys. Rev. B **79**, 064103 (2009).
[17] D. Murali, B. K. Panigrahi, M. C. Valsakumar, S. Chandra, C. S. Sundar, and B. Raj, J. Nucl. Mater. **403**, 113 (2010).
[18] E. Wang, J. Cheng, J. Ma, H. Wu, J. Chen, K. Chou, and X. Hou, Metall. Mater. Trans. A **49**, 5169 (2018).
[19] A. R. Setiawan, M. Hanafi Bin Ani, M. Ueda, K. Kawamura, and T. Maruyama, ISIJ Int. **50**, 259 (2010).
[20] J. Takada and M. Adachi, J. Mater. Sci. **21**, 2133 (1986).
[21] R. Idczak, Appl. Phys. A **122**, 1009 (2016).
[22] X. Zhang *et al.*, Current Applied Physics **18**, 183 (2018).
[23] X. Wang, M. Posselt, and J. Faßbender, Phys. Rev. B **98**, 064103 (2018).
[24] L. R. Velho and R. W. Bartlett, Metall. Mater. Trans. B **3**, 65 (1972).

[25] R. A. Perkins and R. A. Padgett, Acta Metall. **25**, 1221 (1977).
[26] A. J. Ross, H. Z. Fang, S. L. Shang, G. Lindwall, and Z. K. Liu, Comput. Mater. Sci. **140**, 47 (2017).
[27] J. J. Kim, S. H. Shin, J. A. Jung, K. J. Choi, and J. H. Kim, Appl. Phys. Lett. **100**, 131904 (2012).
[28] O. Senninger, F. Soisson, E. Martínez, M. Nastar, C.-C. Fu, and Y. Bréchet, Acta Mater. **103**, 1 (2016).
[29] J. Wu, S. D. Zhang, W. H. Sun, Y. Gao, and J. Q. Wang, Corrosion Science **136**, 161 (2018).
[30] H. Asteman, J.-E. Svensson, L.-G. Johansson, and M. Norell, Oxid. Met. **52**, 95 (1999).
[31] G. Kresse and J. Furthmüller, Comput. Mater. Sci. **6**, 15 (1996).
[32] P. E. Blöchl, Phys. Rev. B **50**, 17953 (1994).
[33] G. Kresse and D. Joubert, Phys. Rev. B **59**, 1758 (1999).
[34] J. P. Perdew, K. Burke, and M. Ernzerhof, Phys. Rev. Lett. **77**, 3865 (1996).
[35] M. Methfessel and A. T. Paxton, Phys. Rev. B **40**, 3616 (1989).
[36] H. J. Monkhorst and J. D. Pack, Phys. Rev. B **13**, 5188 (1976).
[37] A. Claisse and P. Olsson, Nucl. Instrum. Methods Phys. Res., Sect. B **303**, 18 (2013).
[38] G. Henkelman, B. P. Uberuaga, and H. Jónsson, J. Chem. Phys. **113**, 9901 (2000).
[39] L. Qin and C. Jiang, Int. J. Hydrogen Energy **37**, 12760 (2012).
[40] B. Puchala and D. Morgan, Phys. Rev. B **85**, 064106 (2012).
[41] A. Van der Ven, G. Ceder, M. Asta, and P. D. Tepesch, Phys. Rev. B **64**, 184307 (2001).
[42] D. Hlushkou, K. N. Knust, R. M. Crooks, and U. Tallarek, J. Phys.: Condens. Matter **28**, 194001 (2016).
[43] M. E. Tuckerman, *Statistical Mechanics: Theory and Molecular Simulation* (Oxford University Press, United Kingdom, 2010).
[44] R. Soulairol, C.-C. Fu, and C. Barreteau, J. Phys.: Condens. Matter **22**, 295502 (2010).
[45] G. H. Vineyard, J. Phys. Chem. Solids **3**, 121 (1957).
[46] D. E. Jiang and E. A. Carter, Phys. Rev. B **67**, 214103 (2003).
[47] C. Barouh, T. Schuler, C.-C. Fu, and T. Jourdan, Phys. Rev. B **92**, 104102 (2015).
[48] S. Choudhury, D. Morgan, and B. P. Uberuaga, Sci. Rep. **4**, 6533 (2014).
[49] D. P. Whittle and G. C. Wood, J. Electrochem. Soc. **115**, 133 (1968).
[50] M. Reyes, A. Aryanfar, S. W. Baek, and J. Marian, J. Nucl. Mater. **509**, 550 (2018).
[51] J.-H. Ke, E. R. Reese, E. A. Marquis, G. R. Odette, and D. Morgan, Acta Mater. **164**, 586 (2019).